

# Efficient Learning of Accurate Surrogates for Simulations of Complex Systems

A. Diaw<sup>1,2,\*</sup>, M. McKerns<sup>1,\*</sup>, I. Sagert<sup>1</sup>, L. G. Stanton<sup>3</sup>, and M. S. Murillo<sup>4</sup>

<sup>1</sup>Los Alamos National Laboratory, Los Alamos, NM, USA

<sup>2</sup>RadiaSoft LLC, Boulder, CO, USA

<sup>3</sup>Department of Mathematics and Statistics, San José State University, San José, CA, USA

<sup>4</sup>Department of Computational Mathematics, Science and Engineering, Michigan State University, East Lansing, Michigan 48824

\*corresponding: diaw@lanl.gov; mmckerns@lanl.gov

## ABSTRACT

Machine learning methods are increasingly used to build computationally inexpensive surrogates for complex physical models. The predictive capability of these surrogates suffers when data are noisy, sparse or time-dependent. As we are interested in finding a surrogate that provides valid predictions of any potential future model evaluations, we introduce an online learning method empowered by optimizer-driven sampling. The method has two advantages over current approaches. First, it ensures that all turning points on the model response surface are included in the training data. Second, after any new model evaluations, surrogates are tested and “retrained” (updated) if the “score” drops below a validity threshold. Tests on benchmark functions reveal that optimizer-directed sampling generally outperforms traditional sampling methods in terms of accuracy around local extrema, even when the scoring metric favors overall accuracy. We apply our method to simulations of nuclear matter to demonstrate that highly accurate surrogates for the nuclear equation of state can be reliably auto-generated from expensive calculations using few model evaluations.

## 1 Introduction

Surrogate models are essential in science and engineering for modeling and optimizing systems that are too computationally expensive to handle directly. For example, climate modeling, quantum information science, and automated instrumentation control all require alternatives to expensive simulations for robust predictions<sup>1–4</sup>. Crucially, surrogates should have guarantees that they faithfully predict the system’s behavior, including phenomena like phase transitions. Macroscopic simulations in materials science<sup>5</sup> rely on closure information based on data from microphysical methods such as molecular dynamics<sup>6,7</sup> or Monte Carlo<sup>8</sup>. However, typical data is high-dimensional, noisy, sparse, and possibly time-dependent. Producing sufficient data requires a prohibitively large number of microscopic calculations leading to potential roadblocks for materials discovery and design and the robust prediction of material properties<sup>9,10</sup>.

A common strategy is to accompany the surrogate evaluation with an uncertainty metric that determines whether new fine-scale simulations are needed. Such an approach has been applied by Lubbers et al.<sup>11</sup> and Diaw et al.<sup>12</sup>, who apply active learning to generate surrogates of fine-scale material response. Roehm et al.<sup>13</sup> used kriging to construct surrogates of stress fields and communicate the results to a fine-scale code that solves the macro-scale conservation laws for elastodynamics. Noack et al.<sup>4</sup> used a similar kriging-based approach to construct surrogates for autonomous X-ray scattering experiments. They used a genetic algorithm to find the maximum of the variances for each measured data point, and then drew new samples from a distribution that is localized around the solved

maximum. None of these studies ensures that the surrogates are valid on future data: there is no guarantee of surrogate validity.

We propose an online learning methodology to efficiently construct surrogates that are *asymptotically* valid for any future data as defined in Methods 4.1; details of this claim are discussed in the modeling section. Our methodology has three key components: (1) a sampling strategy to generate new training and test data, (2) a learning strategy to generate candidate surrogates from the training data, and (3) a validation metric to evaluate candidate surrogates against the test data. Radial basis function (RBF) interpolation<sup>14–16</sup> are used as the surrogate estimator’s response surface. The numerical realization is done with *mystic*, an open-source optimization, learning, and uncertainty quantification toolkit<sup>17,18</sup>. Our online approach is designed to include the turning points in the search criteria, and thus we conjecture that the training set need only include the turning points. The intended design should yield a negligible increase in retraining times.

The current work primarily focuses on how sampling strategy affects the efficiency when producing an asymptotically valid surrogate. Here, we characterize validity via the evolution of the surrogate test score. Figure (1) shows the procedure to create such a surrogate for an expensive model; it is iterative and includes explicit validation and update mechanisms. To reduce computational complexity, we first link the model to a database (DB); thus, the input and output of the model are automatically stored when it is evaluated. Later, the DB of model evaluations is used to train candidate surrogates. When the model is evaluated, the corresponding surrogate is

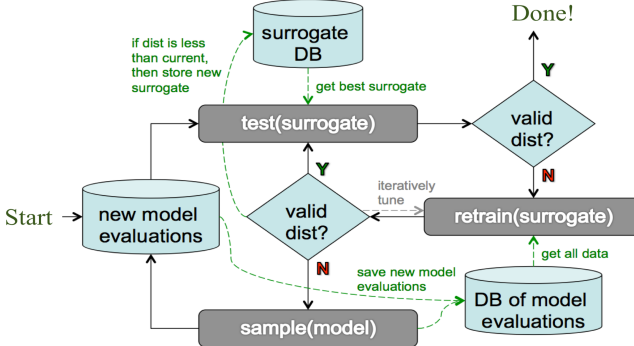


**Figure 1.** Schematic for the automated generation of computationally inexpensive surrogates for a complex physical system. When new model evaluations occur, the corresponding surrogate is retrieved and evaluated for the same data. If the surrogate is determined to still be valid, the execution stops. Otherwise, the surrogate is updated by retraining against the DB of stored model evaluations, where the surrogate is validated with a fine-tuning of surrogate hyperparameters against a quality metric. If iterative retraining improves the surrogate, it is saved. Otherwise, new model evaluations are sampled to generate additional data. The process repeats until testing produces a valid surrogate.

retrieved from the surrogate DB and tested for validity. If no stored surrogate exists, we skip testing and proceed directly to learning a candidate surrogate.

## 2 Results

We first assess the performance of sampling strategies against benchmark functions, which is then extended to finding accurate surrogates for equation-of-state (EOS) calculations of dense nuclear matter. A second application of radial distribution functions in strongly coupled plasmas is given in the Supplement.

### 2.1 Numerical evaluation: benchmark functions

Our case studies use several benchmark functions that are commonly applied to test the performance of numerical optimization algorithms. We first examine how the sampling strategy affects the efficiency and effectiveness of finding an asymptotically valid surrogate. Then, we explore how the optimizer configuration impacts the efficiency of generating an initial valid surrogate.

**Sampling for Asymptotic Validity.** Here, we compare the abilities of optimizer-directed sampling and random sampling to find an accurate surrogate for all future data. We use the workflow for asymptotic validity, as defined in Methods 4.1, to learn a surrogate for the  $d$ -D Rastrigin function<sup>19</sup>:

$$f(\mathbf{x}) = 10d + \sum_{i=1}^d [x_i^2 - 10 \cos(2\pi x_i)], x_i \in [0, 10] \quad (1)$$

with  $d = 2$ , which is a spherical function with an added cosine modulation that produces regularly distributed local minima. Our optimizer-directed sampler uses a “sparsity” sampling strategy with an ensemble of 16 Nelder-Mead solvers.

We define our *test* for validity as:

$$(\text{ave}(\Delta_y) \leq \text{tol}_{\text{ave}}) \wedge (\max(\Delta_y) \leq \text{tol}_{\text{max}}), \quad (2)$$

where  $\wedge$  denotes “and”,  $\text{tol}_{\text{ave}} = 10^{-5}$ ,  $\text{tol}_{\text{max}} = 10^{-4}$ ,  $\Delta_x \neq 0$  is a graphical distance, and *data* corresponds to all existing model evaluations (i.e. prior plus newly sampled). For *train* we also use Eq. (2) with  $\text{tol}_{\text{ave}} = 10^{-5}$  and  $\text{tol}_{\text{max}} = 10^{-4}$ . A quality *metric* for training is given by  $\delta = \sum_y \Delta_y$  and we define *converged* as:

$$\Omega(M) \vee \left( \max_y \left( \max_j \text{ave}(\Delta_{y,j}) \right) \leq \text{tol}_{\text{stop}} \right), \quad (3)$$

where  $\vee$  denotes “or”, and  $\Omega(M)$  is equal to “true” when no new local extrema have been found in the last  $M = 3$  iterations. We use  $\text{tol}_{\text{stop}} = 2 \cdot 10^{-4}$ ,  $\Delta_{y,i}$  is the graphical distance to the *data* sampled in iteration *i* (i.e. no prior model evaluations), and *j* is given by the last  $N = 3$  iterations  $j \in [i - N + 1, \dots, i]$ . By using *warm* = 1000, we ensure that at least 1000 model evaluations are performed per iteration. In addition, we track the testing score for a single iteration *i*:

$$\text{score} = \text{ave}_y(\text{ave}(\Delta_{y,i})), \quad (4)$$

but do not use it to terminate the calculation. To assess stricter tolerances, we repeat the calculation with  $\text{tol}_{\text{ave}} = 10^{-7}$ ,  $\text{tol}_{\text{max}} = 10^{-6}$ , and  $\text{tol}_{\text{stop}} = 2 \cdot 10^{-6}$ . We will refer to these tolerance settings as “strict” and the prior tolerance settings as “loose”.

We compare our results with pure systematic random sampling, using an ensemble of 500 points, for both strict and loose tolerances. As shown in Figures 2 and in Table 5, the test score for pure systematic random sampling converges, yielding an excellent representation of truth faster than optimizer-directed sampling (when using the default optimizer configuration and a metric based on the average surrogate misfit) for both strict and loose tolerances. Because the Rastrigin function has uniformly-distributed, shallow extrema, we expect a systematic random sampling strategy that efficiently covers input space to be more performant than a strategy that attempts to pinpoint the extrema.

We perform a similar comparison for the Rosenbrock function<sup>20</sup>. Its 2-D version is a saddle with an inverted basin that contains a long, narrow, and shallow parabolic valley with a global minimum. The 8-D Rosenbrock function is the sum of seven coupled 2-D functions, with a global minimum at  $x_i = 1$  and local minima near  $x = [-1, 1, \dots, 1]$ . In general, the saddle in the 2-D Rosenbrock function is captured well with either systematic random or optimizer-directed sampling as shown in Fig. (3). Random sampling again converges quicker for strict and loose tolerances (see Table 5). However, upon closer inspection in Fig. (3), we find that optimizer-directed

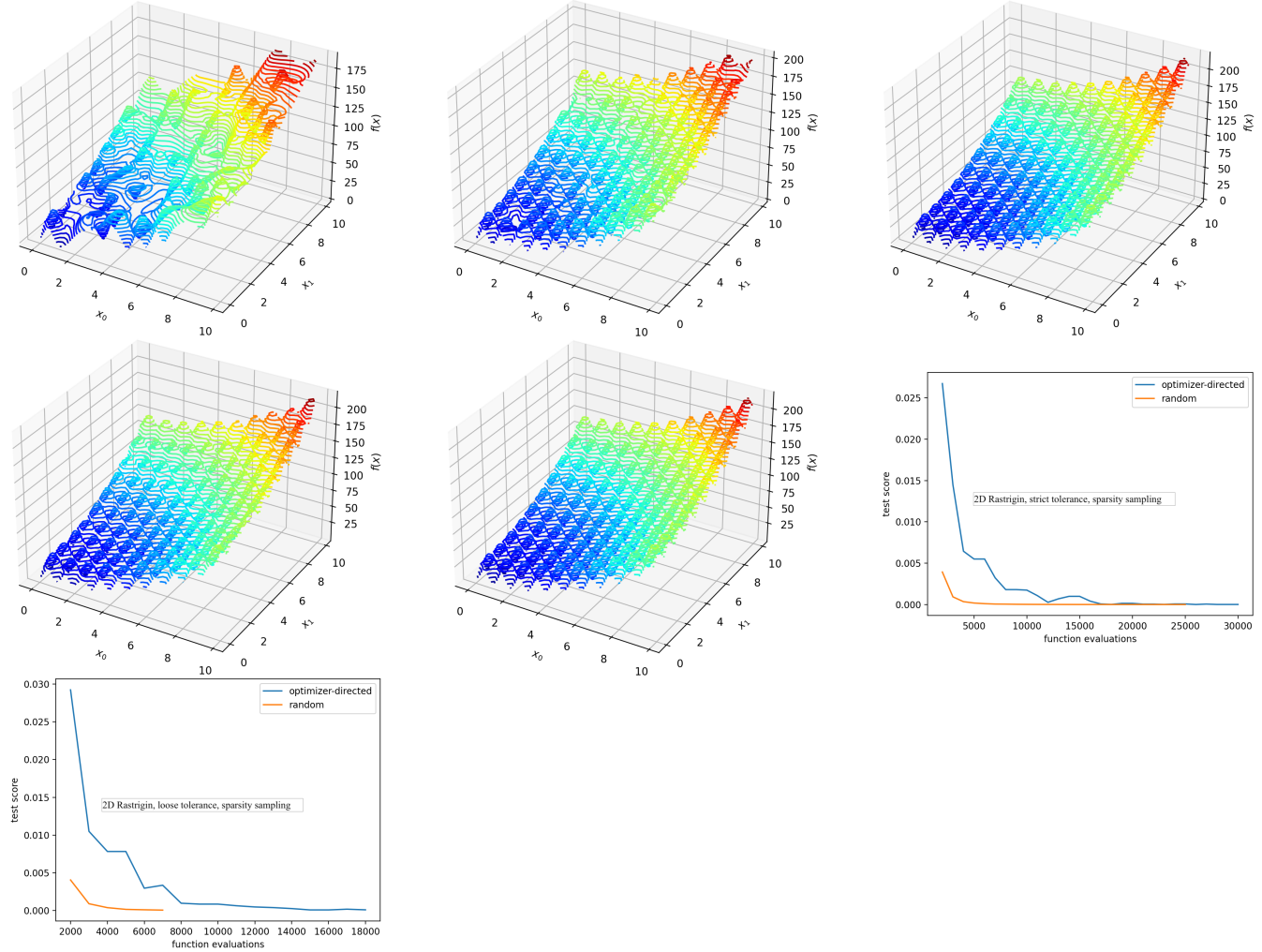


**Figure 2.** Candidate surrogates for the 2-D Rastrigin function, learned with a thin-plate RBF estimator using “sparsity” sampling, a “strict” tolerance, and a test metric for validity based on the average graphical distance between the learned surrogate and sampled data. Surrogates are plotted with inputs  $x = (x_0, x_1)$  and output  $z = f(x)$ . Top row: Sampling using ensembles of 16 optimizers, after the initial, tenth, and final iteration. The final surrogate is visually identical to truth, and the surrogate reproduces all local extrema within the desired accuracy. Bottom row: Sampling using ensembles of 500 points, after the initial and tenth iteration. Mid row, right:: convergence of *test* score versus model evaluations using “sparsity” sampling and a test metric for validity based on the average graphical distance between the learned surrogate and sampled data. (left): “loose” tolerance (right):“strict” tolerance. Note that the test score for pure systematic random sampling converges faster than optimizer-directed sampling, as may be expected for a metric based on the average surrogate misfit.

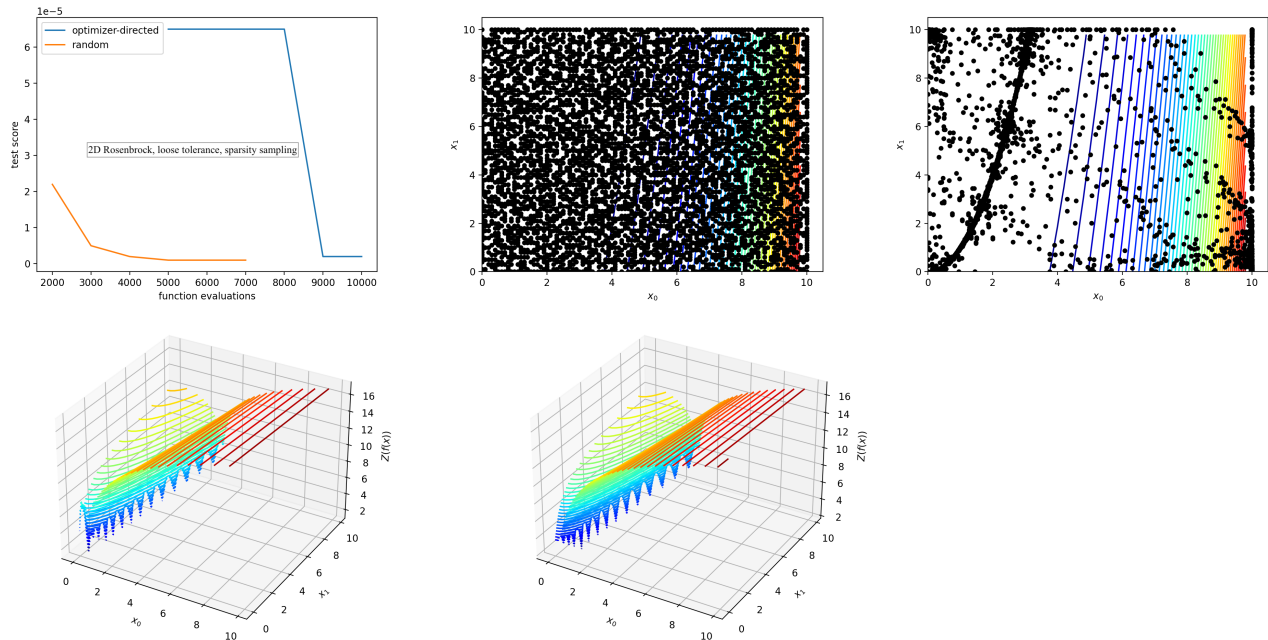


**Figure 3.** Candidate surrogates for the 2-D Rosenbrock function, learned with a thin-plate RBF estimator using “sparsity” sampling, a “loose” tolerance, and a test metric for validity based on the average graphical distance between the learned surrogate and sampled data. Surrogates are plotted with inputs  $x = (x_0, x_1)$  and output  $z = Z(f(x))$ , where log-scaling  $Z = \log(4 \cdot f(x) + 1) + 2$  is used to better view the region around the global minimum. Top row, left: convergence of test score versus model evaluations for 2-D Rosenbrock function at strict tolerance. Top row, middle: model evaluations sampled with the random sampling strategy. Top row, right: optimizer-directed sampling. Bottom row, left: log-scaled view of surrogate from random sampling. Bottom row, right: log-scaled view of surrogate from optimizer-directed sampling, which reproduces truth. Note convergence occurs quickly using either strategy, where the *converged* condition is met with no more than two iterations.

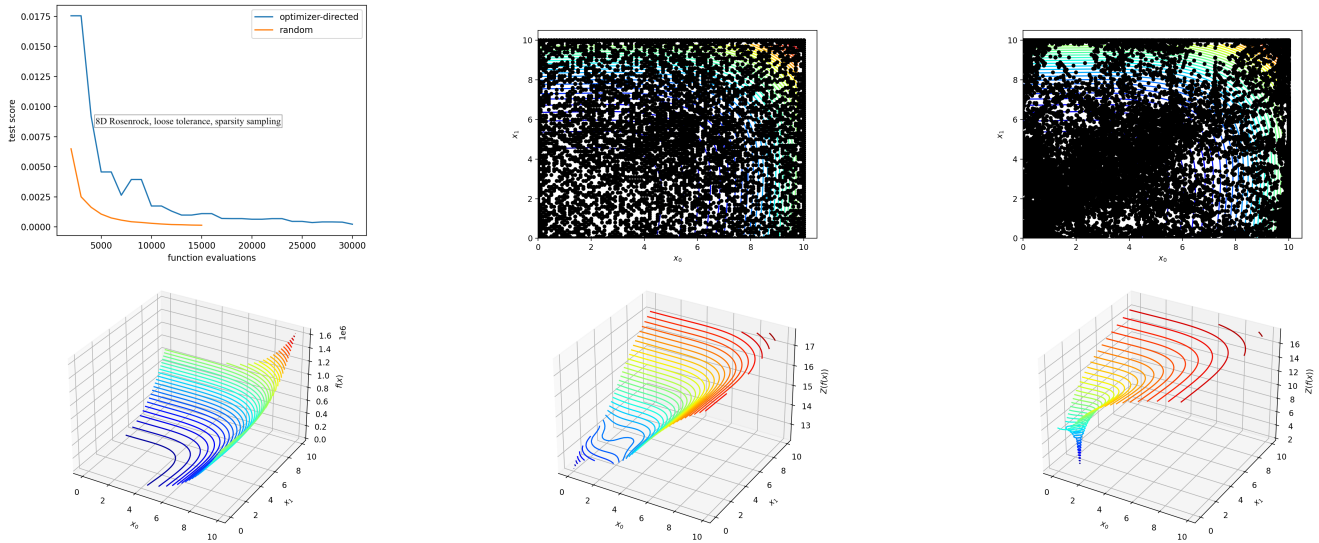


**Figure 4.** Candidate surrogates for the 8-D Rosenbrock function, learned with a thin-plate RBF estimator using “sparsity” sampling, a “loose” tolerance, and a test metric for validity based on the average graphical distance between the learned surrogate and sampled data. Surrogates are plotted with inputs  $x = (x_0, x_1, 1, 1, 1, 1, 1, 1)$  and output  $z = f(x)$  or  $z = Z(f(x))$ , where log-scaling  $Z = \log(4 \cdot f(x) + 1) + 2$  is used to better view the region around the global minimum. Top row, left: test score per sample. Top row, center: model evaluations sampled with the random sampling strategy. Top row, right: optimizer-directed sampling. Bottom row, left: surrogates produced with either sampling approach are visually identical to the truth. Bottom row, center: log-scaled view of surrogate from random sampling near the global minimum. Bottom row, right: log-scaled view of surrogate from optimizer-directed sampling near the global minimum, identical to the truth. Note that while pure systematic random sampling converges faster, optimizer-directed sampling provides a more accurate surrogate near the critical points.

sampling reproduces truth much more accurately in the region surrounding the global minimum. This is a direct consequence of the optimizer-directed strategy that provides a higher sampling density in the neighborhood of the minimum. We find this behavior for strict and loose tolerances and reproduce it for the 8-D Rosenbrock function with loose tolerances (see Figure 4).

For all tested benchmark functions, systematic random sampling is found to converge faster to a valid surrogate. However, optimizer-directed sampling was found to be superior in reproducing the behavior of the benchmark function at its extrema. This finding is well aligned with our conjecture that the minimum data set necessary to produce a highly accurate surrogate is one composed of evaluations located at all turning points of the model’s response surface. In all cases, the Nelder-Mead solver was used in the default configuration. We expect that less strict convergence requirements will reduce the number of required evaluations, potentially at the cost of some accuracy in the vicinity of the extrema. We explore the impact of optimizer configurations in the next section.

**Sampling for Training Validity.** Here, we assess the impact of the optimizer configuration on the efficiency of optimizer-directed sampling. Our sampler uses a lattice sampling strategy with an ensemble of 40 optimizer instances. We define our *test* for validity as:

$$\sum_y \Delta_y \leq tol_{sum} \wedge \max(\Delta_y) \leq tol_{max}, \quad (5)$$

where  $tol_{sum} = 10^{-3}$  and  $tol_{max} = 10^{-6}$ . We use a graphical distance with  $\Delta_x \neq 0$ , and *data* defined as all existing model evaluations (i.e. prior plus newly sampled). We define *train* as in Eq. (5), again with  $tol_{sum} = 10^{-3}$  and  $tol_{max} = 10^{-6}$ . Finally, we use a quality *metric* for training, given by  $\delta = \sum_y \Delta_y$ , and define *converged* identically to *test*. The lattice sampler is configured with the number of bins in each dimension, so  $n_s = (2, 2, 2)$  produces a grid with two bins in each dimension. However, specifying only the number of bins (e.g.,  $n_s = 8$ ), will generate  $n_s$  bins randomly gridded.

To understand the impact of the optimizer configuration, we examined the minimization of the 6-D Hartmann’s function in the region bounded by  $\mathbf{x} \in [-1, 1]$ . The function has a global minimum,  $f(\mathbf{x}) = -3.322$ , that occurs at  $\mathbf{x} = (0.20169, 0.15001, 0.4768, 0.2753, 0.311, 0.6573)$ . Figure (5) shows plots of the convergence of (top) the inputs and (bottom) the output, for the 6-D Hartmann’s function. The results depicted were obtained using a “lattice” sampling strategy with an ensemble of optimizers. Our ensemble was built with a Nelder-Mead solver in the default configuration. This solver will stop when the absolute difference in both  $\mathbf{x}$  and  $f(\mathbf{x})$  over one iteration is less than  $10^{-4}$ , while the latter solver will stop when the normalized absolute difference of  $f(\mathbf{x})$  over 2 iterations is less than  $10^{-4}$ . In Fig. (5), the cost appears to converge by the second iteration and remains unchanged for roughly ten subsequent iterations before the solver terminates. Hence, we should be able to reduce the

number of model evaluations by roughly an order of magnitude with some tuning of the termination conditions.

The 6-D Hartmann’s function (and similarly, the 2-D Easom’s function) provides a challenge for optimizers in that they evaluate to zero everywhere, except in the region around one or more sharp wells. Gradient-based optimizers do not navigate a flat surface well, so some inefficiency should be expected for optimizer-directed sampling for these functions. While again, optimizer-directed sampling (at the default optimizer configuration and for a metric based on the average surrogate misfit) converges less quickly, the difference is not as lopsided as one might anticipate. As seen in Fig. (5), optimizer trajectories generally are short, and terminate quickly in the flat region; however, the region around a well has a higher density than random sampling. The result is that optimizer-directed sampling again produces a better representation of truth near the extrema. Note that for the 6-D Hartmann’s function, optimizer-directed sampling does not capture the behavior of truth exactly around the rim of the well. This is due to our first-order simplification of the methodology searching for extrema, as opposed to all turning points of the response surface. Had we included the turning points in the search criteria, we expect the surrogate would do better at reproducing truth at the rim of the well.

The following section will test the ability to quickly produce a valid surrogate that reproduces relevant physical behavior in regions where traditional methods have difficulty producing similar results. We will use a larger ensemble of optimizers and test the accuracy at the end of a single iteration of our entire workflow. This does not guarantee the surrogate will be valid against all future data, but instead, will give us an idea of how quickly the surrogates can accurately reproduce physical effects near the turning points.

## 2.2 Equation of State with Phase Transition

We consider building an accurate surrogate for a high-density nuclear-matter equation of state (EOS) that contains a phase transition (PT) as an illustrative example. (A second application is described in the Supplement.) Reliable models for nuclear matter exist up to baryon number densities  $n_b$  of about twice the nuclear saturation density  $n_0 \sim 0.16 \text{ fm}^{-3}$  as well as asymptotically high densities of  $n_b > 40 n_0$ <sup>21,22</sup>. While at low densities and temperatures  $T$ , nuclear matter is composed of neutrons and protons, for high values of  $n_b$  and  $T$  it is expected to undergo a transition to matter composed of deconfined quarks and gluons<sup>23</sup>. There are large uncertainties regarding the critical temperatures and densities for the onset of the quark phase, giving motivation for heavy-ion experiments<sup>24–26</sup> and neutron-star research<sup>27–33</sup> to study nuclear matter under extreme conditions. Corresponding numerical studies need a nuclear EOS, either in analytic or tabulated form<sup>34–36</sup>.

To create EOS tables over a large density and temperature range, the most common approach is to select models for the hadronic and quark EOSs and connect them via a Maxwell or

Function	ndim	Random		Optimizer-directed	
		loose	strict	loose	strict
Easom	2	2000	8000	2939	17967
Rosenbrock	2	2000	7000	7317	12111
Rastrigin	2	7000	25000	18579	32308
Michalewicz	2	30000	—	30696	—
Hartmann	6	11000	—	26411	—
Rosenbrock	8	15000	—	31487	—

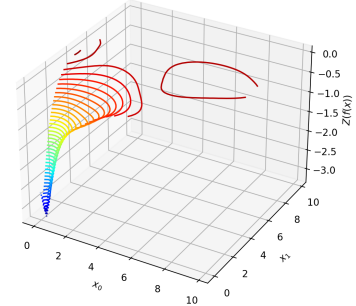
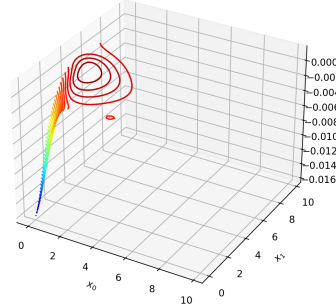
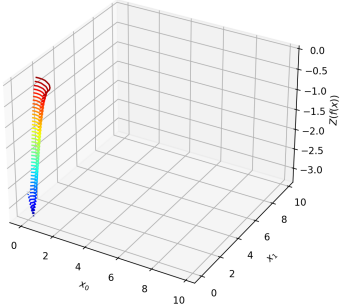
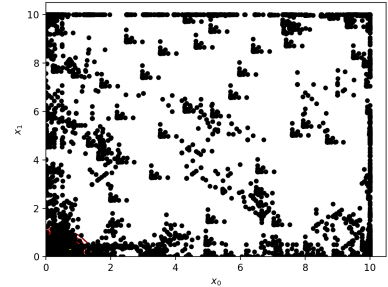
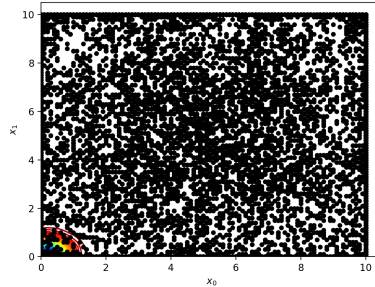
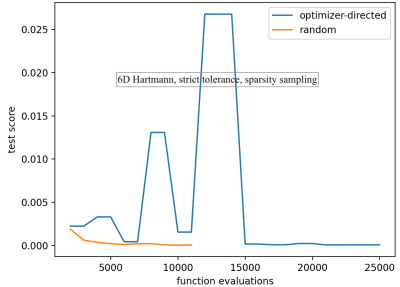
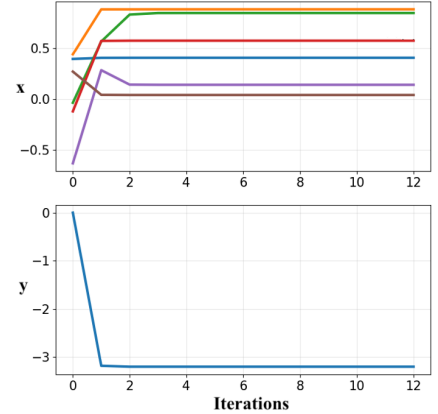


**Figure 5.** Top row, left: Number of evaluations required for several benchmark functions to reach  $tol_{stop}$  for both “loose” and “strict” tolerances, using a sparsity sampler with bounds  $\mathbf{x} \in [0, 10]$ . Top row, right: Convergence of (top) the input parameters  $\mathbf{x}$ , and (bottom) output  $y = f(\mathbf{x})$ , for the 6D Hartmann function, using a Nelder-Mead solver in the default configuration. Note that convergence in  $f(\mathbf{x})$  is reached within the first two iterations. Thus, with some tuning to the termination conditions, we expect an additional order of magnitude efficiency may be achieved. We found similar results using a Powell solver. b) Middle and bottom rows: Same as in Fig. 4 for 6-D Hartmann function. Surrogates are plotted with inputs  $\mathbf{x} = (x_0, x_1, 0.476874, 0.275332, 0.311652, 0.6573)$ . Note the spikes during convergence for optimizer-directed sampling, due to a ‘dramatic’ update to the surrogate. The ‘dramatic’ updates occur when sampling occurs in the region around  $x_i = 2$ , and better shape the transition from the flat region to the entry of the well.

Gibbs construction to represent the PT<sup>37–39</sup>. The Gibbs construction assumes the coexistence of quarks and hadrons in a mixed phase where conservation laws are fulfilled globally. For the Maxwell construction, only baryon number is conserved globally. Other conservation laws, like electric charge neutrality, are fulfilled separately for quark and hadronic matter. Neither of these constructions is currently ruled out; in fact, there are other models to connect the pure hadronic and quark phases, for example via a so-called crossover<sup>23,40</sup>. However, the Maxwell construction usually leads to the most extreme PT characteristics, including a pressure plateau in the mixed phase. With that, it represents a suitable challenge for a surrogate.

We model the PT with the Maxwell construction (see the Supplement). The quark matter EOS is described by the MIT bag model where quarks are non-interacting fermions confined into nucleons at low densities via a confinement pressure, or the so-called bag constant<sup>39,41</sup>, taken here to be 170 MeV. Quark matter is composed of up, down, and strange quarks, which we take to have masses  $m_{\text{up}} = m_{\text{down}} = 0$  and  $m_{\text{strange}} = 150\text{MeV}$ . Nuclear EOS tables for astrophysics are often divided into different temperature blocks with each block containing  $y_p$  sub-blocks in which the thermodynamic quantities are provided for a range of densities. For our demonstration, we assume the pressure to be a function of  $n_b$  and  $y_p$  only, corresponding to a zero-temperature block. The typical range for  $y_p$  in nuclear EOSs is  $0.01 \leq y_p \leq 0.6$ . In order to capture the PT, we focus on densities in the range  $0.04\text{ fm}^{-3} \leq n_b \leq 1.6\text{ fm}^{-3}$ .

We use lattice sampling with an ensemble of 40 Nelder-Mead solvers at the default configuration, and a surrogate learned using a thin-plate RBF. Here, we defined *test* validity as in Eq. (5) with  $\text{tol}_{\text{max}} = 10^{-6}$  and  $\text{tol}_{\text{sum}} = 10^{-3}$ , and *train*, *converged*, *data*, and *metric* as defined in Section 2.1. The results are plotted in Fig. (6a), which shows the entire  $n_b$ - $y_p$  plane, where the pressure plateau of the PT is clearly visible. As seen in previous studies, the critical density for the onset of the mixed phase moves to higher values for increasing  $y_p$ <sup>39</sup>. Fig. (6b) gives a more detailed view of the EOS by showing the pressure profiles for fixed  $y_p$ . As can be seen, no systematic errors arise in the predicted values of the pressure with either proton fraction or density.

Note that the RBFs will reproduce the phase transition accurately if enough of the inflection points of the response surface are sampled. As the optimizers discover all the turning points in the surface (here, the points in the discontinuity), the surrogates also begin to reproduce these discontinuities. We illustrated this point in Fig. (6c) for  $n_b = 0.3$  and  $y_p = 0.3$ . As we increase the size of the ensemble of solvers  $n_s$  directed to find the turning points, the accuracy of the surrogate obtained from a single learning step using a thin-plate RBF improves.

### 3 Conclusion

We presented an online learning strategy designed to produce valid surrogates for a chosen quality metric. The approach

works well in generating surrogates for existing data and can also be applied with regard to future data. We demonstrated an application of online learning where the selection of training data is done with a sampling strategy and an iterative approach is applied to improve surrogate validity versus the chosen metric.

We gave evidence that if the turning points of the model's response surface are known, a robust estimator (e.g. thin-plate RBF interpolation or a MLP neural network) should be able to create a surrogate that reproduces the behavior of more expensive model exactly. We presented an optimizer-directed sampling strategy that is effective at sampling the turning points of a model's response surface. We then compared the efficiency of different sampling strategies in learning surrogates that are valid for benchmark functions, even in the presence of newly sampled data. Note that if the surrogate was found to be invalid for newly acquired data, our online approach can be used to improve it iteratively.

We used a sparse sampling approach for selected benchmark functions that produced new draws at the least-populated points in parameter space. We compared this to an optimizer-directed approach where each initial draw is used as starting point for an optimizer that runs to termination. At first blush, it seemed that the traditional sampling strategy outperformed the optimizer-directed one for all benchmark functions (see Table 5). However, we used a metric that was based on the error in the surrogate's predicted value versus truth, averaged out over the entire response surface. Hence, it should not be surprising that our methodology produced surrogates that are, on average, of high quality across the entire parameter range. One might conclude that a traditional sampling strategy, especially one that provides more diffuse sampling than an optimizer-directed strategy, is more efficient at generating valid surrogates when the average misfit across parameter space measures the validity. We note that the default optimizer configuration was used in testing the efficiency of the sampling strategy, and *tuning* the optimizer may make a substantial difference in the efficiency of the optimizer-directed strategy.

We also noted that our metric made no guarantee regarding the quality of the surrogate *in the neighborhood of the turning points*. Returning to our conjecture, finding a response surface's turning points is key to guaranteeing the long-term validity of the surrogate as new data is collected.

We found that an optimizer-directed approach is superior at minimizing the model error in the neighborhood of the turning points (see Fig. 4), even when the metric does not call for that explicitly. Conversely, a traditional sampling strategy is blind to the response surface and demonstrates a much larger misfit near the turning points. Thus, using a metric that judges the quality of the surrogate by the misfit at the turning points should produce high-quality surrogates with an optimizer-directed approach with even greater efficiency.

For a physical system, the turning points of a response surface are usually associated with the occurrence of new

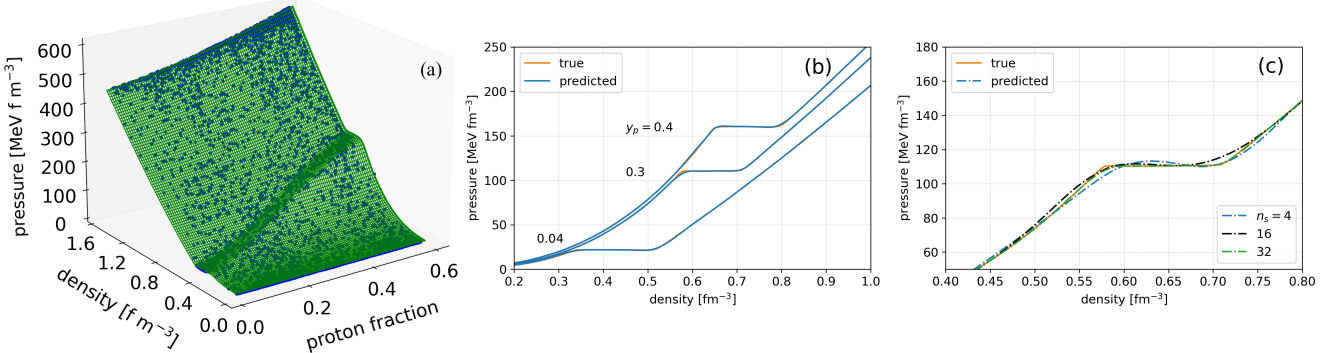


**Figure 6.** (a) Simulations (dots) and predicted values (surface) of the nuclear matter EOS. The initial search domain  $n_b \in [0.04 \text{ fm}^{-3}, 1.2 \text{ fm}^{-3}]$  and  $y_p \in [0.01, 0.6]$  was sampled with a lattice sampler. We used  $n_s = 40$  Nelder-Mead solvers and *test* validity defined as in Eq. (5) with  $tol_{max} = 10^{-6}$ ,  $tol_{sum} = 10^{-3}$ , and *train*, *converged*, *data*, and *metric* as defined in Methods 2.1. A valid surrogate for the EOS that correctly describes the pressure plateau was found after 6846 model evaluations. (b) Pressure as a function of density for given proton fractions  $y_p = 0.04, 0.3, 0.4$ . (c) Pressure as a function of density for  $n_b = 0.3$ ,  $y_p = 0.3$ , and three different sizes of ensembles ( $n_s$ ). The orange curve shows the results from more expensive simulation and the blue curve represents prediction using our methodology. Note as we increase the size of the ensemble of solvers directed to find the turning points, the accuracy of the surrogate obtained from a single learning step using a thin-plate RBF improves. Note the tolerances are absolute, and defined in Eq. (2) with respect to the graphical distance, with  $\Delta x \neq 0$ .

phenomena. This provides additional motivation to reduce the misfit near the turning points as much as possible. With that, we applied our methodology to two physics test problems. We showed that we could efficiently learn surrogates for equation-of-state calculations of dense nuclear matter, yielding excellent agreement between the surrogate and model for a wide parameter range and a region that includes a phase transition. We also showed that our methodology can produce highly-accurate surrogates for radial distribution functions from expensive molecular dynamics simulations for neutral and charged systems of several dimensions and across an extensive range of thermodynamic conditions (given in the Supplement). While our demonstrations were focused on two specific problems, the methodology and associated code are agnostic to the domain science and can be utilized for a wide variety of physics scenarios.

A standard metric that is used to determine the validity of a surrogate is the model error, which is typically a distance such as  $\delta = \sum_y \Delta_y$ , or more generally

$$\delta = metric(\hat{y}(\mathbf{x}|\xi), data) \quad (6)$$

with *metric* being a distance function between the surrogate and all model evaluations, *data*. This definition assesses the quality of the surrogate by measuring its distance from the observed data. Unfortunately, for a small set of observed data that is not representative, any learned surrogate will likely become invalidated with the addition of new data. A potentially more robust assessment of quality considers training a surrogate with a statistical metric, such as the *expected* model error. It can be defined to take into account any knowledge about the data-generating distributions (for input and output values) and any uncertainty in the input and output parameters of the model. Complex real-world models are often

non-deterministic; thus, an appropriate goal is to either find a surrogate that is guaranteed to be accurate under uncertainty or a surrogate that is guaranteed to be robust under uncertainty. With some minor adjustments, such as adding a timestamp strategy or invalidating training data, our methodology can be leveraged to build and maintain accurate surrogates for time-dependent models. In future work, we will apply our methodology to produce surrogates that are guaranteed to be either accurate or robust under uncertainty and similarly demonstrate the ability to guarantee the accuracy of surrogates for time-dependent models.

## 4 Methods

### 4.1 Surrogate Validity.

Our general procedure to create a valid surrogate for an expensive model is shown in Fig. (1). The steps are iterative and include explicit validation and update mechanisms. To simplify computational complexity, we first link the model to a DB. Thus, when the model is evaluated, its inputs and output are automatically stored. The DB of model evaluations is used later to train candidate surrogates. The corresponding surrogate is retrieved from the surrogate DB and tested for validity during model evaluation. If no stored surrogate exists, then we skip testing and proceed directly to learning a candidate surrogate. Validity is defined as

$$test(\Delta) \text{ is true} \quad (7)$$

where *test* is a function of the graphical distance,  $\Delta$

$$\begin{aligned} \Delta_y &= \inf_{\mathbf{x} \in \mathcal{X}} |\hat{y}(\mathbf{x}|\xi) - y| + \Delta_x, \\ \Delta_x &= |\mathbf{x} - \mathbf{x}'| \text{ or } 0 \end{aligned} \quad (8)$$

with  $(\mathbf{x}', y)$  a point in the DB of model evaluations, and  $\mathcal{X}$  the set of all valid inputs  $\mathbf{x}$  for the surrogate  $\hat{y}$  with hyperparameters  $\xi$ .  $\Delta_x$  and  $\Delta_y$  are the pointwise  $\Delta$  for  $(\mathbf{x}', y)$ . If  $\Delta_x = 0$ , we ignore the distance of the inputs while  $\Delta_y$  is the minimum vertical distance of point  $y$  from the surrogate.

If Eq. (7) deems the surrogate to be valid, the execution stops. Otherwise, we update the surrogate by training against the DB of stored model evaluations. We define validity when training a surrogate similar to Eq. (7), but with the function *train* replacing *test*.

We train the surrogate in terms of a quality metric given in Eq. (6). If after training a surrogate has a smaller  $\delta$  compared to the current best surrogate, then we store the updated surrogate in the surrogate DB and continue to improve the surrogate until *train* is satisfied. In the case that training ultimately fails to produce a valid surrogate, we use a sampler to generate model evaluations at new  $(\mathbf{x}', y)$  and the process restarts.

Our general procedure for producing a valid surrogate is extended for asymptotic validity by adding a validity convergence condition

$$\text{converged}(\Delta) \text{ is true} \quad (9)$$

to be called after the surrogate is deemed *test* valid, as in Eq. (7). Thus, instead of stopping execution when the surrogate is *test* valid, the latter merely completes an iteration. If not *converged*, we trigger a new iteration by sampling new data and continue to iterate until the surrogate validity has *converged*. This iterative procedure is more likely to generate a surrogate that is valid for all future data when Eq. (9) requires some form of convergence behavior for *test* over several iterations. This is one of the main innovation of our approach. When the DB of model evaluations is sparsely populated, we expect that any new data will likely trigger a surrogate update.

## 4.2 Learning Strategy.

Our procedure is online, as a sampler can request new model evaluations on-the-fly, which populate to a DB, and our surrogate is updated by querying the DB and training on the stored model evaluations. Online learning is greatly facilitated by automation of the learning process. Our general procedure for automating the production of a valid surrogate is shown in Fig. (1), and is extended to asymptotic validity. As mentioned earlier, we will use a RBF interpolation to generate our surrogates, where we leverage *mystic* for the automation and quality assurance of surrogate production. The utilization of RBFs arises from their universal capabilities for function approximation and their connection to single hidden-layer feed-forward neural networks (NN) with non-sigmoidal nonlinearities<sup>15, 16, 42</sup>. Although a multilayer perceptron (MLP)<sup>43</sup> or another similar NN estimator are also potential choices, we will use RBF interpolation as it is generally more efficient for online learning<sup>15</sup>.

Let us assume  $y(\mathbf{x})$  is an arbitrary function of vector  $\mathbf{x}$  represented on a subset of  $\mathbb{R}^n$ , and that the value of  $y$  at input

vectors  $\mathbf{x}^j$  ( $j = 1, \dots, N$ ) are the known *data* points stored in a DB of model evaluations. We seek to find a surrogate  $\hat{y}(\mathbf{x})$  with the lowest possible number of the evaluations<sup>44–46</sup> satisfying Eq. (6). We use Eq. (6), with  $\mathbf{x}' = \mathbf{x}$ , as opposed to

$$\hat{y}(\mathbf{x}^j) = y(\mathbf{x}^j) \text{ for all } j = 1, \dots, N \quad (10)$$

as we allow our interpolated surrogates to deviate from the data slightly, due to the use of *smooth* and *noise*. Using a RBF  $\phi(r)$ , the interpolated surrogate can be written as:

$$\hat{y}(\mathbf{x}) = \sum_{j=1}^N \beta_j \phi(d(\mathbf{x}, \mathbf{x}^j)), \quad (11)$$

where  $\beta_j$  are coefficients to be determined, the thin-plate ( $\phi = r^2 \ln(r)$ ) RBF is used and  $d(\mathbf{x}, \mathbf{x}^j)$  is a distance function similar to Eq. (6). If we choose  $d(\mathbf{x}, \mathbf{x}^j) = \|\mathbf{x} - \mathbf{x}^j\|$  as the Euclidean distance between an arbitrary vector  $\mathbf{x}$  and  $\mathbf{x}^j$ , the values of the coefficient vector  $\beta = [\beta_1, \beta_2, \dots, \beta_N]^T$  are determined by solving the linear system,  $\mathbf{M}\beta = \mathbf{Y}$ , where  $\mathbf{M}$  is an  $N \times N$  symmetric matrix with elements  $M_{ij} = \phi(\|\mathbf{x}^i - \mathbf{x}^j\|)$ , and  $\mathbf{Y} = [y(\mathbf{x}^1), y(\mathbf{x}^2), \dots, y(\mathbf{x}^N)]^T$ . To prevent issues due to singular matrix  $\mathbf{M}$ , and to provide some randomness in each learned surrogate, we add a very small amount of Gaussian noise to the input data.

## 4.3 Sampling Strategy.

Sampling is an integral part of our online learning workflow and is used to generate new data points  $(\mathbf{x}', y)$  that help inform the learning algorithm whenever training fails to produce a valid surrogate. As the goal is an asymptotically valid surrogate, we also use sampling to kick-start a new iteration after Eq. (7) deems the current iteration's surrogate to be valid (see Fig. (1)). While our workflow's sampling and learning components are fundamentally independent and can run asynchronously, they are linked through the DB of stored model evaluations. The data points generated by the sampler are populated to the DB, while the learning algorithm always uses the data contained in the DB when new training is requested. If there were no concerns about minimizing the number of model evaluations, we could have samplers run continuously, feeding model evaluations into the DB. However, as described above, we explicitly include sampling as part of the iterative workflow to minimize the number of model evaluations.

We conjectured that (given the training data) a learned surrogate that, at a minimum, includes all of the turning points of a response surface  $y(\mathbf{x})$  is guaranteed to be valid for all future data. Thus, we postulate that a sampling strategy that uses *optimizer-directed* sampling will be most efficient in discovering all the turning points of  $y(\mathbf{x})$ . We distinguish *optimizer-directed* sampling from *traditional* sampling. Optimizer-directed sampling uses an optimizer to direct the sampling toward a goal. In contrast, traditional methods, such as simple random sampling generally ignore the response of  $y(\mathbf{x})$ . The utility of simple random sampling is that all the samples will draw (with replacement) from a distribution, and thus all sample points can be chosen simultaneously.

Subsequently,  $y(\mathbf{x})$  can be evaluated in parallel for all points drawn in the sampling. An optimizer-directed approach uses traditional sampling to generate samples for the first draw, then uses each first draw member as a starting point for an optimizer that will direct the sampling of the second and subsequent draws toward a turning point on the response surface. When an optimizer's termination condition is met, traditional sampling is again used to generate a new starting point for a new optimizer, which then proceeds to termination as above. Thus, while an optimizer-directed strategy may be less efficient in generating new data points, it should be more efficient at finding the turning points of the response surface, and thus be the preferred strategy when a surrogate is required to be asymptotically valid.

## 5 Code availability

The code, as well as the sampled data and learned surrogates, will be available soon on Code Ocean.

## 6 Acknowledgments

Research supported by Los Alamos National Laboratory under the Laboratory Directed Research and Development program (project numbers 20190005DR, 20200410DI, and 20210116DR), by the Department of Energy Advanced Simulation and Computing under the Beyond Moore's Law Program, and by the Uncertainty Quantification Foundation under the Statistical Learning program. Triad National Security, LLC operates the Los Alamos National Laboratory for the National Nuclear Security Administration of the U.S. Department of Energy (Contract No. 89233218CNA000001). The authors thank Jeff Haack for insightful feedback on the manuscript. This document is LA-UR-20-24947.

## 7 Author contributions statement

A.D., M.M., and M.S.M. conceived the project. M.M. developed the software. A.D., I.S., and M.M. performed simulations and prepared figures. All authors were responsible for the formal analysis.

## 8 Additional information

**Competing financial interests:** The authors declared no competing financial interests.

## References

1. Barros, V. *et al.* (eds.) *Climate Change 2014 Impacts, Adaptation, and Vulnerability* (Cambridge University Press, New York, 2014).
2. Wigley, P. *et al.* Fast machine-learning online optimization of ultra-cold-atom experiments. *Sci. Reports* **6** (2016).
3. Scheinker, A. & Gessner, S. Adaptive method for electron bunch profile prediction. *Phys. Rev. Accel. Beams* **18** (2015).
4. Noack, M. *et al.* A kriging-based approach to autonomous experimentation with applications to x-ray scattering. *Sci. Reports* **9** (2019).
5. Coveney, P. V., Boon, J. P. & Succi, S. Bridging the gaps at the physics-chemistry-biology interface. *Philos. Transactions Royal Soc. Lond. Ser. A* **374**, 20160335 (2016).
6. Hu, S. X. *et al.* First-principles thermal conductivity of warm-dense deuterium plasmas for inertial confinement fusion applications. *Phys. Rev. E* **89**, 043105, DOI: [10.1103/PhysRevE.89.043105](https://doi.org/10.1103/PhysRevE.89.043105) (2014).
7. Stanton, L. G., Glosli, J. N. & Murillo, M. S. Multiscale molecular dynamics model for heterogeneous charged systems. *Phys. Rev. X* **8**, 021044 (2018).
8. Brown, E. W., Clark, B. K., DuBois, J. L. & Ceperley, D. M. Path-integral monte carlo simulation of the warm dense homogeneous electron gas. *Phys. Rev. Lett.* **110**, 146405 (2013).
9. Schmidt, J., Marques, M., Botti, S. & Marques, M. Recent advances and applications of machine learning in solid-state materials science. *npj Comput. Mater.* **5** (2019).
10. Liu, Y., Zhao, T., Ju, W. & Shi, S. Materials discovery and design using machine learning. *J. Materomics* **3** (2017).
11. Lubbers, N. *et al.* Modeling and scale-bridging using machine learning: nanoconfinement effects in porous media. *Sci. Reports* **10**, 13312 (2020).
12. Diaw, A. *et al.* Multiscale simulation of plasma flows using active learning. *Phys. Rev. E* **102**, 023310 (2020).
13. Roehm, D. *et al.* Distributed Database Kriging for Adaptive Sampling (D<sup>2</sup> KAS). *Comput. Phys. Commun.* **192**, 138–147 (2015).
14. Coulomb, J.-L., Kobetski, A., Caldora Costa, M., Maréchal, Y. & Jonsson, U. Comparison of radial basis function approximation techniques. *COMPEL-The international journal for computation mathematics electrical electronic engineering* **22**, 616–629 (2003).
15. Wu, Y., Wang, H., Zhang, B. & Du, K.-L. Using radial basis function networks for function approximation and classification. *ISRN Appl. Math.* **2012** (2012).
16. Park, J. & Sandberg, I. W. Universal approximation using radial-basis-function networks. *Neural computation* **3**, 246–257 (1991).
17. McKerns, M., Hung, P. & Aivazis, M. mystic: highly-constrained non-convex optimization and UQ (2009). <http://pypi.python.org/pypi/mystic>.

18. McKerns, M., Strand, L., Sullivan, T. J., Fang, A. & Avazis, M. Building a framework for predictive science. In *Proceedings of the 10th Python in Science Conference*, 67–78 (2011). <http://arxiv.org/pdf/1202.1056>.

19. Rastrigin, L. A. *Systems of External Control* (Mir Publishers, Moscow, 1974). (in Russian).

20. Rosenbrock, H. An automatic method for finding the greatest or least value of a function. *The Comput. J.* **3**, 175–184 (1960).

21. Lonardoni, D., Tews, I., Gandolfi, S. & Carlson, J. Nuclear and neutron-star matter from local chiral interactions. *Phys. Rev. Res.* **2**, 022033, DOI: [10.1103/PhysRevResearch.2.022033](https://doi.org/10.1103/PhysRevResearch.2.022033) (2020).

22. Annala, E., Gorda, T., Kurkela, A., Nättälä, J. & Vuorinen, A. Evidence for quark-matter cores in massive neutron stars. *Nat. Phys.* DOI: [10.1038/s41567-020-0914-9](https://doi.org/10.1038/s41567-020-0914-9) (2020).

23. Baym, G. *et al.* From hadrons to quarks in neutron stars: a review. *Reports on Prog. Phys.* **81**, 056902, DOI: [10.1088/1361-6633/aaae14](https://doi.org/10.1088/1361-6633/aaae14) (2018).

24. Adam *et al.*, J. Nonmonotonic energy dependence of net-proton number fluctuations. *Phys. Rev. Lett.* **126**, 092301, DOI: [10.1103/PhysRevLett.126.092301](https://doi.org/10.1103/PhysRevLett.126.092301) (2021).

25. Busza, W., Rajagopal, K. & van der Schee, W. Heavy ion collisions: The big picture and the big questions. *Annu. Rev. Nucl. Part. Sci.* **68**, 339–376, DOI: [10.1146/annurev-nucl-101917-020852](https://doi.org/10.1146/annurev-nucl-101917-020852) (2018). <https://doi.org/10.1146/annurev-nucl-101917-020852>.

26. Braun-Munzinger, P., Koch, V., Schäfer, T. & Stachel, J. Properties of hot and dense matter from relativistic heavy ion collisions. *Phys. Reports* **621**, 76–126, DOI: <https://doi.org/10.1016/j.physrep.2015.12.003> (2016). Memorial Volume in Honor of Gerald E. Brown.

27. Raaijmakers, G. *et al.* Constraints on the dense matter equation of state and neutron star properties from nicer’s mass–radius estimate of psr j0740+6620 and multimessenger observations. *The Astrophys. J. Lett.* **918**, L29, DOI: [10.3847/2041-8213/ac089a](https://doi.org/10.3847/2041-8213/ac089a) (2021).

28. Capano, C. D. *et al.* Stringent constraints on neutron-star radii from multimessenger observations and nuclear theory. *Nat. Astron.* **4**, 625–632, DOI: [10.1038/s41550-020-1014-6](https://doi.org/10.1038/s41550-020-1014-6) (2020). [1908.10352](https://doi.org/10.1038/s41550-020-1014-6).

29. Dietrich, T. *et al.* Multimessenger constraints on the neutron-star equation of state and the Hubble constant. *Science* **370**, 1450–1453, DOI: [10.1126/science.abb4317](https://doi.org/10.1126/science.abb4317) (2020). [2002.11355](https://doi.org/10.1126/science.abb4317).

30. Riley *et al.*, T. E. A nicer view of psr j0030+0451: Millisecond pulsar parameter estimation. *The Astrophys. J.* **887**, L21, DOI: [10.3847/2041-8213/ab481c](https://doi.org/10.3847/2041-8213/ab481c) (2019).

31. Miller *et al.*, M. C. Psr j0030+0451 mass and radius from nicer data and implications for the properties of neutron star matter. *The Astrophys. J.* **887**, L24, DOI: [10.3847/2041-8213/ab50c5](https://doi.org/10.3847/2041-8213/ab50c5) (2019).

32. Dexheimer, V. Tabulated neutron star equations of state modelled within the chiral mean field model. *Publ. Astron. Soc. Aust.* **34**, DOI: [10.1017/pasa.2017.61](https://doi.org/10.1017/pasa.2017.61) (2017).

33. Abbott *et al.*, B. Gw170817: Observation of gravitational waves from a binary neutron star inspiral. *Phys. Rev. Lett.* **119**, DOI: [10.1103/physrevlett.119.161101](https://doi.org/10.1103/physrevlett.119.161101) (2017).

34. Typel, S., Oertel, M. & Klähn, T. CompOSE CompStar online supernova equations of state harmonising the concert of nuclear physics and astrophysics compose.obspm.fr. *Phys. Part. Nucl.* **46**, 633–664, DOI: [10.1134/S1063779615040061](https://doi.org/10.1134/S1063779615040061) (2015).

35. Schneider, A. S., Constantinou, C., Muccioli, B. & Prakash, M. Akmal-Pandharipande-Ravenhall equation of state for simulations of supernovae, neutron stars, and binary mergers. *Phys. Rev. C* **100**, 025803, DOI: [10.1103/PhysRevC.100.025803](https://doi.org/10.1103/PhysRevC.100.025803) (2019).

36. Raithel, C. A., Özal, F. & Psaltis, D. Finite-temperature Extension for Cold Neutron Star Equations of State. *Astrophys. J.* **875**, 12, DOI: [10.3847/1538-4357/ab08ea](https://doi.org/10.3847/1538-4357/ab08ea) (2019).

37. Glendenning, N. K. *Compact Stars: Nuclear Physics, Particle Physics and General Relativity*. Astronomy and Astrophysics Library (Springer New York, 1997).

38. Hempel, M., Pagliara, G. & Schaffner-Bielich, J. Conditions for phase equilibrium in supernovae, protoneutron, and neutron stars. *Phys. Rev. D* **80**, 125014, DOI: [10.1103/PhysRevD.80.125014](https://doi.org/10.1103/PhysRevD.80.125014) (2009).

39. Fischer, T. *et al.* Core-collapse supernova explosions triggered by a quark-hadron phase transition during the early post-bounce phase. *The Astrophys. J. Suppl. Ser.* **194**, 39, DOI: [10.1088/0067-0049/194/2/39](https://doi.org/10.1088/0067-0049/194/2/39) (2011).

40. McLellan, L. & Reddy, S. Quarkyonic matter and neutron stars. *Phys. Rev. Lett.* **122**, 122701, DOI: [10.1103/PhysRevLett.122.122701](https://doi.org/10.1103/PhysRevLett.122.122701) (2019).

41. Chodos, A., Jaffe, R. L., Johnson, K., Thorn, C. B. & Weisskopf, V. F. New extended model of hadrons. *Phys. Rev. D* **9**, 3471–3495, DOI: [10.1103/PhysRevD.9.3471](https://doi.org/10.1103/PhysRevD.9.3471) (1974).

42. Rocha, H. On the selection of the most adequate radial basis function. *Appl. Math. Model.* **33**, 1573–1583 (2009).

43. Rumelhart, D. E., Hinton, G. E. & Williams, R. J. Learning internal representations by error propagation. In *Parallel Distributed Processing: Explorations in the Microstructure of Cognition*, 318–362 (MIT press Cambridge, MA, 1986).

44. Schaback, R. & Wendland, H. Adaptive greedy techniques for approximate solution of large RBF systems. *Numer. Algorithms* **24**, 239–254 (2000).

45. Rocha, H. On the selection of the most adequate radial basis function. *Appl. Math. Model.* **33**, 1573 – 1583 (2009).
46. Dorvlo, A. S., Jervase, J. A. & Al-Lawati, A. Solar radiation estimation using artificial neural networks. *Appl. Energy* **71**, 307 – 319 (2002).